Drift Phase Structure Implications for Radiation Belt Transport

For submission to JGR Space Physics

T.P. O'Brien[1], J.C. Green[2], A.J. Halford[1,4], B.P. Kwan[1], S.G. Claudepierre[1,5], and Louis G. Ozeke[3]

[1]Space Sciences Department, The Aerospace Corporation, El Segundo, California, USA.
[2]Space Hazards Applications, LLC, Golden, Colorado, USA
[3]Department of Physics, University of Alberta, Edmonton, Alberta, Canada.
[4]Now at NASA Goddard Spaceflight Center, Greenbelt, Maryland, USA
[5]Now at University of California, Los Angeles, California, USA

Corresponding Author: T. Paul O'Brien
14301 Sullyfield Circle, Unit C, CH1-515
Chantilly, VA, 20151
paul.obrien@aero.org

Running Title: DRIFT PHASE STRUCTURE

Key Points:

- Some radial transport mechanisms produce drift phase structure
- Drift phase structure is not strongly associated with electron belt enhancements
- Drift resonance with random-phase broadband waves appears to dominate

Abstract

We examine drift phase structure in the electron radiation belt observations to differentiate radial transport mechanisms. Impulsive electrostatic or electromagnetic fields can cause radial transport and produce drift echoes (periodic drift phase structures with energy-dependent period). Narrow-band standing electromagnetic wave fields can also cause radial transport, while producing energy-independent periodic drift phase structures. Broad-band, random-phase electromagnetic wave fields can cause radial transport, but do not necessarily produce drift phase structure. We present results of three case studies showing little association between drift phase structure and ~MeV electron flux enhancements in the outer belt. We estimate the amplitude of drift phase structures expected for impulsive or narrow-band interactions to compete with broad-band, random-phase waves. We show that the observed drift phase structure is typically much smaller than would be present if either impulses or narrow-band waves were the dominant cause of radial transport. We conclude that radial transport is primarily consistent with the broad-band, random-phase, small perturbations assumed in quasilinear diffusion theory, although we cannot rule out the unlikely possibility that radial transport plays little role in radiation belt dynamics.

Plain Language Summary

Radial motion of electrons is one of the most significant processes in the dynamics of the Earth's electron radiation belts. We examine the ripples in the time series of radiation belt electron flux observations to determine how the electrons move radially in space. Different kinds of radial motion leave different signatures in these time series ripples. Large ripples are rare enough that much of the radial reshaping of the radiation belts occurs independent of their influence. Established radial transport theory, known as quasilinear theory, is consistent with many small ripples, but our analysis cannot rule out the unlikely alternative that the small ripples indicate that there is little or no radial transport happening in the radiation belts.

Keywords
Radiation belts, radial transport, radial diffusion, drift resonance, ULF waves

1 Introduction

Radial transport of electrons has long been thought to be an essential component of radiation belt dynamics [*Falthammar* 1965; 1968]. It can be an energization mechanism, when it brings particles from the plasma sheet into the radiation belts while preserving their first and second adiabatic invariants [e.g., *Jaynes et al.*, 2018; *Ozeke et al.*, 2019]. It can also be a loss mechanism, transporting particles outward through the magnetopause [*Shprits et al.*, 2006; *Loto'aniu et al.*, 2010; *Ozeke et al.*, 2020]. While the relevance of transport is apparent, the details of how it occurs and is modeled are still debated. Although radial transport is sometimes clearly impulsive [e.g., *Li et al.*, 1993; *Kress et al.*, 2007; *Foster et al., 2015; Hudson et al.*, 2017; *Patel et al., 2019, Hao et al.*, 2019; *Hudson et al.*, 2020], it is most often represented as a diffusive process in radiation belt simulations [*Boscher et al.*, 1996; *Brautigam and Albert*, 2000; *Elkington et al.*, 2003; *Shprits and Thorne*, 2004; *Fei et al.*, 2006; *Loto'aniu et al.*, 2006; *Subbotin and Shprits*, 2009; *Su et al.*, 2011; *Reeves et al.*, 2012; *Tu et al.*, 2013; *Glauert et al.*, 2014; *Ozeke et al.*, 2020]. In these simulations, radial transport is modeled as diffusive changes in L^*, a form of the third adiabatic invariant associated with azimuthal particle drift around Earth. Some test particle simulations have been used to assess the validity of this representation and support the use of this diffusive approximation [e.g., *Sarris et al.*, 2006; *Huang et al.*, 2010; *Li et al.*, 2016]. However, results from other test particle simulations argue that radial transport is idiosyncratic to each individual geomagnetic storm, and the diffusive approximation only holds in aggregate over many storms [*Chen et al.*, 1992, *Riley and Wolf*, 1992, and *Ukhorskiy et al.* 2005; *Ukhorskiy and Sitnov*, 2006; 2008]. If correct, these results would suggest that substantially different and likely computationally more expensive approaches are required to model the near-Earth radiation environment.

Our goal is to distinguish what general type of transport (diffusive vs. non-diffusive) occurs during radiation belt enhancements using the drift phase structure of the electron flux as a diagnostic tool. Additionally, we will use the drift structure to characterize the details of the transport process and discern between radial transport events caused by impulsive injections and those related to interaction with ultra-low frequency (ULF) waves. To do so requires an understanding of the signatures of each of these processes.

Electrostatic and electromagnetic impulses produce drift phase structure of the electron flux known as drift echoes [*Brewer et al.*, 1969; *Lanzerotti et al.*, 1969; *Schulz and Lanzerotti*, 1974]. These drift echoes are characterized by fluctuations with a period that corresponds to the particle’s drift period. Since the drift period depends on the particle energy, the hallmark of impulsive transport is energy-dispersed drift echoes. Of course, if enough impulses are randomly superimposed on each other within a single drift period, no drift echoes can be observed. However, in this scenario, the impulsive behavior is effectively indistinguishable from the action of broad-band, random-phase power and the diffusive approximation is clearly applicable.

Narrow-band standing electromagnetic waves produce oscillations in particle drift phase structures. In this case, all energies oscillate at the same frequency, but there is an energy-dependent phase shift [*Kokubun et al.*, 1977; *Southwood and Kivelson*, 1981; *Zong et al.*, 2009; *Claudepierre et al.*, 2013; *Chen et al.*, 2017; *Teramoto et al.*, 2019; *Hao et al.*, 2020]. A superposition of many narrow-band waves can smooth out the drift phase structure [*Elkington et al.*, 2003], but, again, this is effectively indistinguishable from broad-band, random-phase power, and the diffusive approximation would be applicable. In fact, a variety of interactions are possible, involving broad and narrow-band waves, with global and limited local time scope [see, e.g., *Hao et al.*, 2019; 2020; *Zhao et al.*, 2021]

In the quasilinear approximation [*Falthammar*, 1965] of diffusion, broad-band, random-phase, small amplitude waves produce many infinitesimal radial transport events over the course of a particle's drift orbit. As this approximation breaks down, either due to large amplitude waves, non-random phase, or narrow-band power, drift phase structure should become more evident.

Using multiple case studies, we will look for evidence in the electron drift-phase structure of non-quasilinear, non-diffusive processes leading to significant transport. We adopt as our null hypothesis that the radial transport is diffusive even on timescales as short as a few hours. We will reject the null hypothesis if, during radiation belt enhancements, we can detect drift phase structures that are often larger than those expected from the quasilinear approximation. Section 2 describes our method for determining the amplitude of drift phase structures that would indicate non-diffusive transport. Section 3 describes the radiation belt data used in the analysis. Section 4 describes the individual events considered. Lastly, section 5 concludes that the rarity of drift phase structures larger than what is implied by diffusion coefficients computed from observed ULF wave power during storms that appear to have significant radial transport, leaves the hypothesis of quasilinear radial diffusion intact.

2 Estimating the Size of Drift Phase Structure

Our null hypothesis is that diffusive quasilinear radial transport, which preserves the first and second adiabatic invariants, is the dominant transport process in the radiation belts. Since diffusive transport is caused by the superposition of many waves or impulses, we expect this type of transport to create some level of fluctuations in the particle flux. In order to differentiate diffusive from non-diffusive transport we must estimate the threshold size (amplitude) of drift phase structures that would indicate non-quasilinear transport. To make this size estimate, we begin with the transport equation:

$$\frac{\partial \bar{f}}{\partial t} = L^2 \frac{\partial}{\partial L}\bigg|_{M,K} \left[\frac{D_{LL}}{L^2}\frac{\partial \bar{f}}{\partial L}\bigg|_{M,K}\right] \qquad (1)$$

In this equation $\bar{f}$ is the phase-averaged phase space density (PSD), and the coordinates are adiabatic invariants [e.g., *Schluz and Lanzerotti*, 1974]:

$$M = \frac{p^2 \sin^2 \alpha}{2 m_0 B} \qquad (2)$$

$$K = \int_{s'_m}^{s_m} \sqrt{B_m - B(s)}\, ds \qquad (3)$$

$$L = L^* = \frac{2\pi\mu_E}{R_E\Phi} \tag{4}$$

M is the first invariant, which depends on the particle's momentum *p*, local pitch angle α, rest mass m_0, and the local magnetic field strength *B*. *K* is the second invariant, which involves an integral of the local field strength *B(s)* relative to the mirror point field strength B_m, with the integral taken along the field line from the southern (s'_m) to northern (s_m) mirror points. Finally, the third invariant *L* depends on the magnetic moment of the Earth (μ_E), Earth's radius (R_E), and the magnetic flux Φ enclosed by the particle's drift orbit. For our analysis, we will use the TS04D magnetic field model [*Tsyganenko and Sitnov*, 2005] to provide *K* and *L*.

2.1 Diffusion coefficient and drift phase structure

The amount of transport in equation (1) is captured in the diffusion coefficient, D_{LL}, and is the focus of our derivation of the size of diffusive and non-diffusive drift structure. It is given by:

$$D_{LL} = \frac{\langle(\Delta L)^2\rangle}{2\Delta t} \tag{5}$$

In essence, D_{LL} arises from a series of wave-particle interactions, separated in time by Δt, that produce changes in *L* that have a variance $\langle(\Delta L)^2\rangle$ over many interactions. If these perturbations conserve PSD (Liouville's theorem) then the PSD amplitude can be related to how far they moved (ΔL) and the radial gradient in PSD $\left.\frac{\partial \bar{f}}{\partial L}\right|_{M,K}$. The quasilinear regime is defined by many such perturbations (small Δt) that are small in amplitude (small $\langle(\Delta L)^2\rangle$) producing a finite D_{LL}.

Schulz and Lanzerotti [1974, section IV.8] estimate an electromagnetic D_{LL} based on magnetic impulses that might be appropriate for quiet time. Their treatment is especially interesting because it derives D_{LL} from the peak-to-peak amplitude of drift echoes. Our estimate of the expected amplitude of drift phase structures applies the same logic, but in reverse – starting from D_{LL}, how large in amplitude should the drift phase structures be to indicate transport in excess of the quasilinear approximation?

We begin our estimate of the expected size of drift phase structure by assuming an initial state in which the PSD is sufficiently mixed in drift phase such that $f_0(M, K, L, \phi_3) = \bar{f}_0(M, K, L)$, where ϕ_3 is the drift phase angle and f_0 has been averaged over bounce- and gyro-phases. We then assume the PSD is perturbed by an interaction with some unspecified electric and magnetic fields that preserve *M* and *K*, but induce a ϕ_3-dependent change in *L*. We denote this change $\Delta L(\phi_3)$, which is the change in *L* as a function of ϕ_3 *after* the interaction. Conservation of phase-space density (Liouville's theorem) provides that the PSD after the interaction is:

$$f_1(M, K, L, \phi_3) = \bar{f}_0(M, K, L - \Delta L(\phi_3)) \tag{6}$$

Figure 1 illustrates this process: the particles carry their initial phase-space density with them as they move in L. Drift phase structure arises because the displacement is phase-dependent. The size of the drift phase structure depends on the displacement in L and the local phase space density gradient (for a statistical investigation of this phenomenon, see *Sarris et al.*, [2021]). As noted by *Hartinger et al.* [2020] if there is no radial gradient in the phase space density, radial transport will not result in drift phase structures, including drift echoes; this is common in the outer zone at ~MeV energies. We must, therefore, be careful to account for the presence *or absence* of a PSD gradient when assessing the expected size of drift phase structure for quasilinear diffusion.

Taking a natural logarithm of (6) and the using a first order Taylor expansion yields:

$$\ln f_1(M,K,L,\phi_3) \cong \ln \bar{f}_0(M,K,L) - \left.\frac{\partial \ln \bar{f}_0}{\partial L}\right|_{M,K} \Delta L(\phi_3) \qquad (7)$$

The PSD gradient $\left.\frac{\partial \ln \bar{f}_0}{\partial L}\right|_{M,K}$ emerges explicitly in the second term of the Taylor expansion.

If we take a drift average ($\langle\cdot\rangle_d$), we have

$$\ln \bar{f}_1(M,K,L) = \langle \ln f_1(M,K,L,\phi_3)\rangle_d \cong \ln \bar{f}_0(M,K,L) - \left.\frac{\partial \ln \bar{f}_0}{\partial L}\right|_{M,K} \langle \Delta L(\phi_3)\rangle_d \qquad (8)$$

The variance is:

$$\langle (\Delta \ln f)^2\rangle_d = \langle \left[\ln f_1(M,K,L,\phi_3) - \ln \bar{f}_1(M,K,L)\right]^2\rangle_d \cong \left(\left.\frac{\partial \ln \bar{f}_0}{\partial L}\right|_{M,K}\right)^2 \langle (\Delta L(\phi_3))^2\rangle_d (9)$$

Over many interactions, $\langle (\Delta L(\phi_3))^2\rangle_d$ should converge to $\langle (\Delta L)^2\rangle$ (i.e., the population variance). Thus, we have

$$\langle (\Delta \ln f)^2\rangle_d \sim \left(\left.\frac{\partial \ln \bar{f}_0}{\partial L}\right|_{M,K}\right)^2 \langle (\Delta L)^2\rangle = \left(\left.\frac{\partial \ln \bar{f}_0}{\partial L}\right|_{M,K}\right)^2 2\Delta t D_{LL} \qquad (10)$$

While this approximation does not hold instantaneously, it does describe the expected magnitude of perturbations for D_{LL} made up of individual perturbation episodes. Left open to interpretation is the time between perturbations, Δt. If Δt is small compared to a drift period, τ_d, then the system is clearly in the quasilinear diffusive regime (many interactions per drift period). However, for values of Δt that are comparable to or larger than τ_d, the system may deviate from the quasilinear ideal. Thus, a signature of the system deviating from the quasilinear regime is

$$\langle (\Delta \ln f)^2\rangle_d > \left(\left.\frac{\partial \ln \bar{f}_0}{\partial L}\right|_{M,K}\right)^2 2\tau_d D_{LL} \qquad (11)$$

when D_{LL} is given by the quasilinear approximation. In other words, this expression sets a floor on the size of drift phase perturbations one would expect to observe if significant non-quasilinear behavior is present. We cannot observe the statistics of the process directly because nature does not provide repeated experiments the way a laboratory does. However, we know that the condition in equation (11) can only be met, if there are sufficient cases of

$$\left|\ln f_1(M,K,L,\phi_3) - \ln \bar{f}_1(M,K,L)\right| > \left|\left.\frac{\partial \ln \bar{f}_0}{\partial L}\right|_{M,K}\right| \sqrt{2\tau_d D_{LL}} \qquad (12)$$

In words, the detrended phase space density, or flux, must exceed the *L* gradient times the expected *L* displacement on a drift timescale, in a root-mean-squared sense. To use equation (12) requires an estimate of D_{LL} from quasilinear theory. There have been many attempts to specify the diffusion coefficient [*Cornwall*, 1968; 1972; *Lanzerotti et al.*, 1970; 1978; *Lanzerotti and Morgan*, 1973; *Lanzerotti and Wolfe*, 1980; *Brautigam and Albert*, 2000; *Huang et al.*, 2010; *Ali et al.*, 2016; *Li et al.*, 2016; *Fei et al.*, 2006; *Lejosne et al.*, 2013; *Ozeke et al.*, 2012,2014; *Ali et al.*, 2015,2016]. We highlight the work of *Fei et al.*, [2006] for a discussion of the challenges in relating conceptual representations of the electric and magnetic components of D_{LL} to practical observations of in situ electromagnetic fields. Ultimately, we adopt the D_{LL} representation of *Ozeke* et al., [2014] as it is based on the most comprehensive ULF wave observations.

Next, we relate the statement about phase-space density drift phase structure in (12) to observed drift phase structure in particle flux.

2.2 Drift phase structure in observed fluxes

A satellite typically observes flux, $j = p^2 f$, as a function of energy (or, equivalently, *p*), local pitch angle (α), and time *t*. From the satellite location $\vec{r}$, the channel energy, and look direction, we can infer the *M*, *K*, *L*, and ϕ_3 coordinates of particles being measured at any time. Thus, we can write:

$$j(p,\alpha,\vec{r}) = p^2 f(M(p,\alpha,\vec{r}), K(\alpha,\vec{r}), L(\alpha,\vec{r}), \phi_3(p,\alpha,\vec{r})) \tag{13}$$

So long as the spacecraft is not moving too fast, we can safely assume that a time average in an energy-pitch angle bin over a drift period along the spacecraft motion is equivalent to a drift average at fixed *M*, *K*, and *L*. That is, in terms of natural logs:

$$\langle \ln j(p,\alpha,\vec{r}(t))\rangle_{\tau_d} \approx 2\ln p + \langle \ln f(M,K,L,\phi_3)\rangle_d \tag{14}$$

With minor manipulations, we can then show that (12) becomes:

$$\left|\ln j(p,\alpha,\vec{r}(t)) - \overline{\ln j}\,(p,\alpha,\vec{r}(t))\right| > \left|\frac{\partial \ln \bar{f}_0}{\partial L}\Big|_{M,K}\right| \sqrt{2\tau_d D_{LL}} = \Delta \ln j \tag{15}$$

Here $\overline{\ln j}$ represents a centered time average taken over at least one drift period. Appendix A provides the procedure for computing $\frac{\partial \ln \bar{f}_0}{\partial L}$ from flux observations. With (15) in hand, we have a tool for relating observed drift phase structure in particle fluxes to the amplitudes $\Delta \ln j$ of the drift phase structures that would be required for non-quasilinear radial transport to dominate over quasilinear radial transport.

3 Data Sources

Our analysis relies on several data sources: in situ particles and fields, a geomagnetic activity index, and ground magnetometers. The in-situ particle and fields come from the *B* spacecraft in NASA's Van Allen Probes mission [*Mauk et al.*, 2013], abbreviated RBSP, for Radiation Belt Storm Probes, its pre-launch designator. The vehicle was in a low inclination orbit, with a roughly 9-hour orbit, having low altitude inclination and an apogee of around 5.8 R_E. The vehicle spin was ~5.5 RPM on an axis that was roughly pointed sunward. The elliptical, low-inclination orbit allowed RBSP-B to sweep through the entire outer radiation belt in a few hours, and it repeated this process twice each orbit, once outbound, and once inbound.

We use the electron flux from the Magnetic Electron Ion Spectrometer (MagEIS) family of sensors [*Blake et al.*, 2013] on RBSP. We use the level 3 data product (release 4), which includes electron flux versus time, energy, and local pitch angle. Every ~11 seconds, there is 2-dimensional record providing flux at fixed energies and local pitch angles. The pitch angle bins are about 15 degrees wide, while the energy bins vary across the sensor range, and energy resolution at ~1 MeV is 10%-30% full-width-half-max (FWHM). Figure 2 shows how drift period depends on L, and how this energy spread translates to spread in drift period for particles in each of the four energy channels we will use. Although MagEIS provides a background-corrected flux for most energy channels, we use uncorrected fluxes because we are working in a region of the outer zone where backgrounds are not large. We also examine MagEIS histogram data products [*Claudepierre et al.*, 2021] which have narrow energy bandwidth, and so provide a potentially sharper view of drift phase structures with larger amplitudes [see, e.g., *Hartinger et al.*, 2018; *Sarris et al.*, 2020]. In particular, we select a histogram channel whose nominal energy is close to the center energy of the main channel for the same pixel so that its flux is directly comparable, with only the energy bandwidth being different.

For context, we examine magnetometer data from the Electric and Magnetic Field Instrument Suite and Integrated Science (EMFISIS) instrument [*Kletzing et al.*, 2013] on RBSP-B. We use a 1-second, level 3 product, which provides magnetometer vectors in the geocentric solar magnetospheric (GSM) coordinate system, with accuracy and resolution of better than 1 nT.

We use the ground-based planetary *Kp* index as inputs to the *Ozeke et al.* [2014] model of D_{LL}. We use the Omni database for *Kp* and hourly interplanetary and geomagnetic conditions [*King and Papitashvili*, 2005]. We also use ground-based magnetometry from the Canadian Array for Realtime Investigations of Magnetic Activity (CARISMA) network [*Mann et al.*, 2008] to compute event-specific D_{LL}. The general procedure for computing D_{LL} is based on *Ozeke et al.* [2014], whereas the details of computing event-specific D_{LL} are given in *Mann et al.* [2016] and *Ozeke et al.* [2017; 2020].

We use these data sets together to examine three magnetic storm events to determine whether the observed drift phase structure in the outer zone is large enough to indicate non-quasilinear radial transport is a significant contributor to outer zone dynamics.

4 Event Study

Because every geomagnetic storm is unique [see, e.g., *Reeves et al.*, 2003], it is necessary to look at several events to gain a sense of whether and how the drift phase structure indicates radial transport is happening. We consider three different events, chosen for data quality and exemplary drift-phase structure. For each event, we provide an overview of geomagnetic conditions and MagEIS observations in time series form. We then slice each event into individual RBSP-B passes through the outer zone. For each pass, we detrend the fluxes to isolate the drift-phase structure. We also compute the expected magnitude of that drift-phase structure, according to (15). We provide the analysis details during the exposition on the first event and will follow the same analysis procedure for the second and third events. We then examine whether the conclusions change using event-specific D_{LL} rather than the parametric climatological D_{LL}.

4.1 June 2013

Our first event is a ~-100 *Dst* magnetic storm that occurred at the end of May / start of June in 2013. Figure 3 provides an overview of the event. The storm activity was driven by a strongly southward interplanetary magnetic field (IMF), and was accompanied by a gradual increase in solar wind speed (Vsw) from <400 km to ~800 km. The event, as is common during storms, consisted of a dropout of relativistic electron flux during the main phase, followed by a gradual recovery. We have selected 4 passes through the belts for further examination, labeled, *a*, *b*, *c*, and *d*, in panel d. For each pass, we use a sixth-order low-pass Butterworth filter [*Butterworth*, 1930] to remove fluctuations with periods shorter than 30 minutes. The filter is applied separately to the natural logarithm of fluxes in each energy channel and pitch angle bin. According to the drift periods in Figure 2, the 30-minute low-passed filtered log flux approximates a drift average $\overline{\ln j}\,(p, \alpha, \vec{r}(t))$ throughout the outer zone. The detrended residual $\ln j(p, \alpha, \vec{r}(t)) - \overline{\ln j}\,(p, \alpha, \vec{r}(t))$ is, therefore, approximately the drift phase structure. (We perform our mathematical manipulations in natural log, but we will follow the established convention of graphing common log fluxes, i.e., $\log_{10} j$.)

Poisson counting noise could produce apparent drift phase structure. In the plots like panel a.ii of Figure 4, we draw dashed gray lines to indicate the total drift phase amplitude, $\sqrt{(\Delta \ln j)^2 + C^{-1}}$, where C represents the number of counts in the flux accumulation. Because we have chosen intervals where the flux is adequate to have minimal Poisson noise, these additional curves are not distinct in the plots.

We consider in detail the drift structures observed during a few passes of the satellite throughout the storm. The first pass, *a*, is of interest because it had a large, impulsive drift phase structure, extending down to L~3, before the dropout. The other passes plotted occur in the middle of a flux increase. Figure 4 panels a.i, a.ii, and a.iii show pass *a* in detail. Panel a.i gives the residual drift phase structure in three energy channels near 1 MeV. The impulse and accompanying drift echoes are evident in the first ~30 minutes of the plot. A region of "ΔL Exclusion" (the horizontal black bar on the border between panels a.i and a.ii) indicates where the change in L over a drift period for a 1 MeV electron is either less than 0.05 or greater than 0.5 – in the marked region, the calculation of $\frac{\partial \ln \bar{f}_0}{\partial L}$ is potentially suspect. Panel a.ii shows the detrended flux in the 1.1 MeV main and histogram channel as well as the detrended total magnetic field (|B|). As with log flux, the detrended |B| is the residual after subtracting a 30-minute Butterworth low-pass filtered |B|. The gray shading indicates $\pm\Delta \ln j$ from (15) converted to common log. For D_{LL} in (15), we evaluate the climatological *Kp*-dependent *Ozeke et al.* [2014] model, which accounts for only electromagnetic perturbations (total electromagnetic ULF wave power). We see that drift phase structure in the fluxes initially follows fluctuations in $|B|$, but then decouples after ~1:00.

Finally, panel a.iii of Figure 4 shows flux versus McIlwain L, where L is obtained from the Olson-Pfitzer Quiet field model [*Olson and Pfitzer*, 1977] for a locally mirroring particle. Three passes are shown, with the orange pass being the one shown in panels a.i and a.ii. The dark blue pass precedes the orange pass, and the light blue pass follows. Gray shading provides the expected amplitude of drift-phase-structure, derived from the smoothed flux and $\pm\Delta \ln j$ from (15) for the orange pass. We can see in panels a.ii and a.iii that the large impulse between L=3 and 4 is not actually large enough to produce radial transport in excess of what is indicated by quasilinear theory and the model D_{LL}. This is a theme we will see throughout our survey of the three events: the drift phase structure rarely extends outside the $\pm\Delta \ln j$ range indicated by quasilinear theory. In this particular case, any flux enhancement caused by the impulse is quickly depleted by other main phase loss processes: the light blue trace in panel a.iii is nearly 2 orders of magnitude down from the orange trace, indicating a sharp drop in flux over ~4 hours.

While pass *a* was chosen because of its large, obvious impulse, we chose passes *b-d* because they occur while the flux is increasing across all L shells. Panels b-d in Figure 4 are in the same format as their counterparts in panel *a*. In all three passes *b-d*, the orange and magenta traces, which represent the detrended flux, almost never reach outside the gray shaded region. This indicates that, although the flux is increasing, the drift phase structure is too small to indicate significant non-quasilinear radial transport. We note that the 1.6 MeV (green) channel is experiencing substantial Poisson noise during this and several of the later intervals under study.

The 1.1 MeV main and histogram channel shown in Figure 4 both have a center energy of 1064 keV. The main channel's energy bandwidth is 309 keV FWHM (29%). The histogram channel's energy bandwidth is 96 keV (9%). Yet the two channels show very similar drift phase structure. The histogram channel does not show larger amplitude or qualitatively different structure, and so it is unlikely that significant structure is being hidden by the width of the main channel. We will see this behavior repeated in the other two events we will examine.

4.2 October 2013

The next event we have chosen to study occurred in early October 2013, as shown in Figure 5. A modest sized storm occurs on October 8^{th} and 9^{th} and recovers over several days. The storm is accompanied by modest southward IMF and a rapid increase in solar wind speed. Again, the relativistic electron flux drops out during the main phase and recovers over the following days. We have selected four passes, labeled *a, b, c*, and *d* in panel d, from the main phase and early recovery phase for detailed examination.

Pass *a* is shown in Figure 6 panels a.i, a.ii, and a.iii, following the same format as Figure 4. We chose pass *a* because of the small impulse observed near L~5 around 20:00 on October 8^{th}. This impulse produced some drift echoes, as can be seen in panel a.i. Panel a.ii shows that the impulse also caused the residual flux to briefly extend outside the $\pm\Delta \ln j$ boundary around 20:20. The associated impulse in $|B|$ indicates that this is an electromagnetic impulse causing rapid radial transport that is stronger than indicated by the quasilinear model. However, panel a.iii shows that as with the impulse in Figure 4, the flux actually goes down significantly in the hours after the impulse, on account of main phase loss processes.

Pass *b*, shown in Figure 6 panels b.i, b.ii, and b.iii, exhibits ongoing drift phase structure that is correlated with fluctuations in the magnetic field. However, the drift phase structure is smaller than what would be required to produce more transport than indicated by the quasilinear D_{LL}. Nonetheless, as shown in panel b.iii, flux is increasing at all L values in the outer zone. Passes *c* and *d*, shown in panels c.i through d.iii show weak drift phase structure, far smaller than $\pm\Delta \ln j$ from D_{LL}. Panel d.i and d.ii show a very clear case of drift relatively weak drift phase structure while the fluxes are increasing over the range L>4.5. Panel d.ii also shows something we see in a number of passes: as we approach a steep L gradient in the flux, the residual of the 30-minute smoothed flux sometimes curves upward or downward and can extend outside the gray shading for $\pm\Delta \ln j$. We interpret these as edge effects on the residual flux calculation, since they are one-sided (i.e., the flux only goes up or down, it does not vary in both directions).

4.3 November 2013

The final event we examine occurred in early November 2013, shown in Figure 7. The event consists of two main phases with *Dst* < -50 nT. The first one is accompanied by stronger southward IMF and is accompanied by a gradual increase in solar wind speed from ~400 km/s to ~600 km/s. The second main phase is smaller and is accompanied by weaker southward IMF. We examined all passes during the entire 4-day interval shown in Figure 7, and selected three from the second *Dst* recovery for more detailed study. These three passes are labeled *a*, *b*, and *c*, in panel d.

Figure 8 shows the three selected passes in detail. Panels a.i, a.ii, and a.iii provide details of pass *a*. Panel a.ii shows some drift phase structure that is correlated with fluctuations in the magnetic field. This drift phase structure is partially reflected in the (noisy) 0.75 and 1.6 MeV channels, suggesting that it is field line motion causing the drift phase structure. However, for the most part, this structure is never large enough to extend outside the gray $\pm\Delta \ln j$ boundaries. Panel a.iii shows that this pass is associated with a drop in the electron flux across the entire outer zone. The next pass, *b*, is shown in panels b.i, b.ii, and b.iii. Panels b.i and b.ii show that this pass is relatively free of drift phase structure. The $\pm\Delta \ln j$ boundaries are fairly narrow in b.ii and b.iii, and yet the flux does not extend outside them much. Where the flux does extend outside the boundaries, it appears to be Poisson fluctuations, rather than genuine drift phase structure. The final pass, *c*, is shown in panels c.i through c.iii. Below L~4.5 there is some drift phase structure, but it stays within the $\pm\Delta \ln j$ boundaries. After crossing L~4.5, the $\pm\Delta \ln j$ boundaries are again fairly narrow, but the drift phase structure is also very narrow. Again, the drift phase structure does not extend outside the boundaries, suggesting whatever radial transport is occurring during these passes is dominated by quasilinear D_{LL}.

4.4 June 2013 – with Event-Specific D_{LL}

Up to this point, we have used a climatological *Kp*-driven D_{LL}, from *Ozeke et al.* [2014]. However, because there is considerable variation in D_{LL} around these climatological models [*Sandhu et al.*, 2021], it is better to use event-specific D_{LL}. It is possible, with some effort, to produce event-specific D_{LL} to use in (15), and we have done so for the first event, May-June 2013. Figure 9 shows the first two passes from Figure 3 and Figure 4. Panels a.i through a.iii are repeated from Figure 3. Panel a.iv shows the climatological D_{LL} and the event-specific D_{LL}. Panels a.v and a.vi show $\pm\Delta \ln j$ boundaries computed with this event-specific D_{LL}. We see that the prior to 01:11, the event-specific D_{LL} is smaller than the climatological D_{LL}, leading to narrow $\pm\Delta \ln j$ boundaries (compare gray shading between panels a.ii and a.v). In this interval, the (electro)magnetic fluctuations cause drift phase structures that do briefly extend outside the gray $\pm\Delta \ln j$ boundaries around L~3.5. However, from 01:11 onward, the drift phase structure remains within the $\pm\Delta \ln j$ boundaries, suggesting a return to the quasilinear radial transport regime. As noted above, any flux enhancement caused by this magnetic impulse is ultimately lost subsequently during the storm main phase, as the flux drops by several orders of magnitude before the next pass through the belts (panels a.iii and a.vi).

Panels b.i through b.vi in Figure 9 show pass b from Figure 3 and Figure 4. Again, the event-specific D_{LL} is smaller than the climatological D_{LL} up to about L~5, as shown in panel b.iv. However, in this pass, the drift phase structures in panel b.v do not extend outside the $\pm\Delta \ln j$ boundaries. Thus, even the somewhat narrower boundaries implied by the weaker D_{LL} do not cause us to reject the hypothesis that radial transport is largely quasilinear.

We examined the other passes shown in Figure 3 and Figure 4, which showed event-specific D_{LL} larger than the climatological model. Thus, those passes also leave the null hypothesis intact.

5 Discussion and Conclusion

Starting with a null hypothesis that radial transport is mainly caused by quasilinear diffusion, we tested that hypothesis against observed drift phase structure across three events. In these three events, the drift phase structure generally does not exceed the amplitudes implied by quasilinear diffusion. This is true whether we use a climatological model of D_{LL} or event-specific D_{LL}.

When drift phase structure occurs that is larger than the quasilinear expectation, it is associated with (electro-)magnetic impulses (see, e.g., Figure 6 panel a.ii and Figure 9 panel a.v). Although it is clearly possible for magnetic impulses to result in radial transport (famously in the March 1991 event [*Li et al.*, 1993]), in the examples we studied, any belt enhancement caused by the transport event was subsequently lost during the main phase of the storm. This seems a likely fate of many impulses driven by storm sudden commencements – the initial pressure pulse may drive dramatic inward radial transport, only to have the transported particles lost during the main phase of the ensuing storm. We suggest that if the impulse is large enough, and the subsequent storm is not too large, an initially transported population may survive the main phase, as happened in March 1991 and other shock events.

In the events we studied, there is very little storm-time drift phase structure observed at ~1 MeV, and what structure is there is not strongly correlated with flux increases. This is entirely consistent with quasilinear radial diffusion – interaction of electrons with broad-band, random-phase ULF power. Formally, we accept the null hypothesis of quasilinear radial diffusion being the primary cause of radial transport. However, there are some limitations to our analysis that are worth discussing.

First, we have worked entirely in fluxes, and have not accounted for the *Dst* effect [*Dessler and Karplus*, 1961]. This effect can lead to decreases or increases in the electron flux through slow changes in the global magnetic field topology without changing the L^* invariant of the electrons. Passes *c* and *d* of the June 2013 event (Figure 3 and Figure 4) are at approximately the same *Dst*; both are in the middle of flux increases, suggesting that, if the increase is due in part to radial transport, it is achieved via quasilinear diffusion.

Second, we have based our analysis on D_{LL} computed from spatially limited observations of the electromagnetic fields. To convert those fields to D_{LL} requires some assumptions about the spatial structure of those fields. It is possible, then, that some as-yet-unidentified deficiency exists in the inferred D_{LL}, causing it to be too large. For example, the azimuthal mode number m of the ULF waves is typically unknown and assumed to be 1. However, Ozeke *et al.* [2014] explored the effects of assuming m=10 instead of m=1 and found this often reduced D_{LL} by around a factor of 2-3. Still, if for some reason the quasilinear D_{LL} is too large, then we are overestimating the corresponding $\pm\Delta \ln j$.

Third, our finite sensor resolution may be masking hidden drift phase structure. The absence of observed drift phase structure arises from drift phase mixing. At a fine scale, this drift phase mixing never truly disappears. It only disappears *in practice* because our sensors cannot resolve the finest scales. Therefore, in the absence of other processes, it is almost a certainty that with sufficiently fine sensor resolution, there will be drift phase structure. However, we investigated this with the MagEIS histogram channel data and did not find a dramatic effect.

Our analysis, then, leaves something of a conundrum. Some test particle simulations have argued that the quasilinear diffusion limit is only achieved when aggregating over many storms [*Chen et al.*, 1992; *Riley and Wolf*, 1992; *Ukhorskiy* 2006; *Ukhorskiy and Sitnov*, 2008; 2012]. For reasons that are not yet clear, the observations contradict those simulations. Notably, the earlier papers left open the possibility that at higher energies, (e.g., above 130 keV at L~3) radial diffusion might be appropriate. Because the real magnetosphere also involves processes that violate the first and second adiabatic invariants, it is also possible that this fine drift phase structure is truly washed out. As noted by *Sorathia et al.* [2018], these sophisticated radial transport models, those that involve test particle tracing in magnetohydrodynamic (MHD) fields, do not yet include processes that violate the first and second adiabatic invariants. Such processes will mix particles together as they move radially, often involving diffusion in the first and second adiabatic invariants, and sometimes also the third [e.g., *O'Brien* 2015]. Gyroresonant wave-particle interactions will act on the energy and pitch-angle gradients created by drift phase structure, eroding that structure more rapidly in direct proportion to the steepness of the gradients, and intermingling particles on different radial transport trajectories. As the community develops models capable of including gyroresonant processes and test particle transport in MHD fields, we expect to gain insight whether gyroresonant process contribute to a more quasilinear radial transport outcome on a storm-by-storm basis, or whether there is some other explanation for why there is less drift phase structure in the data than would be expected from the simulations.

Acknowledgments: The authors thank D.K. Milling and the rest of the CARISMA team for data. CARISMA is operated by the University of Alberta, funded by the Canadian Space Agency. This work was supported by NASA LWS grant NNX14AF99G, and by RBSP-ECT funding provided by JHU/APL contract 967399 under NASA's Prime contract NAS5-01072. MagEIS data are available at www.rbsp-ect.lanl.gov. EMFSIS magnetometer data are available from emfisis.physics.uiowa.edu. Omni data are available at omniweb.gsfc.nasa.gov. CARISMA ground magnetometer data can be obtained at www.carisma.ca. The authors thank I. Mann and A. Boyd for helpful discussions. Data used in this study can be found at doi:10.5281/zenodo.5796400.

Appendix A. **Estimation of PSD gradient from flux**

In this appendix, we will provide the necessary steps to compute $\left.\frac{\partial \ln \bar{f}_0}{\partial L}\right|_{M,K}$ from flux observed as a function of momentum *p*, local pitch angel α, and position $\vec{r}$ along a spacecraft orbit. First, we recognize that the position along the spacecraft trajectory can be replaced with time *t*:

$$j(p,\alpha,t) = j(p,\alpha,\vec{r}(t)) \qquad \text{(A1)}$$

Next, we consider the time average of ln j:

$$\overline{\ln j}\,(p,\alpha,t) \approx \langle \ln j(p,\alpha,\vec{r}(t))\rangle_{\tau_d} \approx 2\ln p + \langle \ln f(M,K,L,\phi_3)\rangle_d \qquad \text{(A2)}$$

Before the impulse, then, we have:

$$\overline{\ln j_0}\,(p,\alpha,t) \approx 2\ln p + \ln \bar{f}_0 \left(M(p,\alpha,t), K(\alpha,t), L(\alpha,t)\right) \qquad \text{(A3)}$$

Taking the three derivatives of $\overline{\ln j_0}$, we have:

$$\left.\frac{\partial \overline{\ln j_0}}{\partial \ln p}\right|_{\alpha,t} \approx 2 + \left.\frac{\partial \ln \bar{f}_0}{\partial \ln M}\right|_{K,L} \left.\frac{\partial \ln M}{\partial \ln p}\right|_{\alpha,t} \qquad \text{(A4)}$$

$$\left.\frac{\partial \overline{\ln j_0}}{\partial \alpha}\right|_{p,t} \approx \left.\frac{\partial \ln \bar{f}_0}{\partial \ln M}\right|_{K,L} \left.\frac{\partial \ln M}{\partial \alpha}\right|_{p,t} + \left.\frac{\partial \ln \bar{f}_0}{\partial K}\right|_{M,L} \left.\frac{\partial K}{\partial \alpha}\right|_{p,t} + \left.\frac{\partial \ln \bar{f}_0}{\partial L}\right|_{M,K} \left.\frac{\partial L}{\partial \alpha}\right|_{p,t} \qquad \text{(A5)}$$

$$\left.\frac{\partial \overline{\ln j_0}}{\partial t}\right|_{p,\alpha} \approx \left.\frac{\partial \ln \bar{f}_0}{\partial \ln M}\right|_{K,L} \left.\frac{\partial \ln M}{\partial t}\right|_{p,\alpha} + \left.\frac{\partial \ln \bar{f}_0}{\partial K}\right|_{M,L} \left.\frac{\partial K}{\partial t}\right|_{p,\alpha} + \left.\frac{\partial \ln \bar{f}_0}{\partial L}\right|_{M,K} \left.\frac{\partial L}{\partial t}\right|_{p,\alpha} \qquad \text{(A6)}$$

This gives us a system of three equations (A4)-(A6) in three unknowns: $\frac{\partial \ln \bar{f}_0}{\partial \ln M}$, $\frac{\partial \ln \bar{f}_0}{\partial K}$, and $\frac{\partial \ln \bar{f}_0}{\partial L}$, with the last being the quantity we desire. The derivatives $\frac{\partial \overline{\ln j_0}}{\partial \ln p}$, $\frac{\partial \overline{\ln j_0}}{\partial \alpha}$, and $\frac{\partial \overline{\ln j_0}}{\partial t}$ are taken numerically from the low-pass-filtered flux observations. The partial derivatives $\left.\frac{\partial \ln M}{\partial \ln p}\right|_{\alpha,t}$ and $\left.\frac{\partial \ln M}{\partial \alpha}\right|_{p,t}$ can be obtained analytically from (2):

$$\left.\frac{\partial \ln M}{\partial \ln p}\right|_{\alpha,t} = 2 \tag{A7}$$

$$\left.\frac{\partial \ln M}{\partial \alpha}\right|_{p,t} = \frac{2}{\tan \alpha} \tag{A8}$$

The derivative $\frac{\partial \ln M}{\partial t}$ depends only on *B(t)* along the spacecraft track:

$$\left.\frac{\partial \ln M}{\partial t}\right|_{\alpha,t} = -\frac{d \ln B}{dt} \tag{A9}$$

The remaining derivatives $\frac{d \ln B}{dt}$, $\frac{\partial K}{\partial \alpha}$, $\frac{\partial L}{\partial \alpha}$, $\frac{\partial K}{\partial t}$, and $\frac{\partial L}{\partial t}$ can be obtained numerically from the magnetic ephemeris files provided by the Radiation Belt Storm Probes Energetic Particle, Composition, and Thermal Plasma (RBSP-ECT) science operations center [*Spence* et al., 2013]. We can, therefore, rewrite (A4)-(A6) as a matrix-vector problem:

$$\begin{pmatrix} \left.\frac{\partial \overline{\ln j_0}}{\partial \ln p}\right|_{\alpha,t} - 2 \\ \left.\frac{\partial \overline{\ln j_0}}{\partial \alpha}\right|_{p,t} \\ \left.\frac{\partial \overline{\ln j_0}}{\partial t}\right|_{p,\alpha} \end{pmatrix} \approx \begin{pmatrix} \left.\frac{\partial \ln M}{\partial \ln p}\right|_{\alpha,t} & 0 & 0 \\ \left.\frac{\partial \ln M}{\partial \alpha}\right|_{p,t} & \left.\frac{\partial K}{\partial \alpha}\right|_{p,t} & \left.\frac{\partial L}{\partial \alpha}\right|_{p,t} \\ \left.\frac{\partial \ln M}{\partial t}\right|_{p,\alpha} & \left.\frac{\partial K}{\partial t}\right|_{p,\alpha} & \left.\frac{\partial L}{\partial t}\right|_{p,\alpha} \end{pmatrix} \begin{pmatrix} \left.\frac{\partial \ln \bar{f}_0}{\partial \ln M}\right|_{K,L} \\ \left.\frac{\partial \ln \bar{f}_0}{\partial K}\right|_{M,L} \\ \left.\frac{\partial \ln \bar{f}_0}{\partial L}\right|_{M,K} \end{pmatrix} \tag{A10}$$

Solving this matrix-vector problem yields $\left.\frac{\partial \ln \bar{f}_0}{\partial L}\right|_{M,K}$ as well as $\left.\frac{\partial \ln \bar{f}_0}{\partial \ln M}\right|_{K,L}$ and $\left.\frac{\partial \ln \bar{f}_0}{\partial K}\right|_{M,L}$.

We note that (A10) is essentially a coordinate transform from a (p, α, t) system to an (M, K, L) system, combined with the PSD to flux conversion (the “-2” on the left-hand side). It relates drift-averaged PSD to time-averaged flux. The transform breaks down when the matrix becomes singular. So, in practice, we exclude such singular points from our analysis.

6 References

Ali, A. F., Elkington, S. R., Tu, W., Ozeke, L. G., Chan, A. A. and Friedel, R. H. W. (2015), Magnetic field power spectra and magnetic radial diffusion coefficients using CRRES magnetometer data. J. Geophys. Res. Space Physics, 120: 973–995. doi: 10.1002/2014JA020419.

Ali, A. F., D. M. Malaspina, S. R. Elkington, A. N. Jaynes, A. A. Chan, J. Wygant, and C. A. Kletzing (2016), Electric and magnetic radial diffusion coefficients using the Van Allen probes data, *J. Geophys. Res. Space Physics, 121*, 9586–9607, doi:10.1002/2016JA023002.

Blake, J. B., et al. (2013), The Magnetic Electron Ion Spectrometer (MagEIS) instruments aboard the Radiation Belt Storm Probes (RBSP) spacecraft, *Space Sci. Rev.*, doi:10.1007/s11214-013-9991-8.

Boscher, D., S. Bourdarie, and T. Beutier, (1996) Dynamic modeling of trapped particles, *IEEE Trans. Nucl. Sci. 43*(2), 416-425.

Brautigam, D. H., and J. M. Albert (2000), Radial diffusion analysis of outer radiation belt electrons during the October 9, 1990, magnetic storm, *J. Geophys. Res., 105*(A1), 291–309, doi:10.1029/1999JA900344.

Brautigam, D. H., G. P. Ginet, J. M. Albert, J. R. Wygant, D. R. Rowl, A. Ling, and J. Bass (2005), CRRES electric field power spectra and radial diffusion coefficients, *J. Geophys. Res., 110*, A02214, doi:10.1029/2004JA010612.

Brewer, H.R., M. Schulz, and A. Eviatar, Origin of drift-periodic echoes in the outer-zone electron flux, J. Geophys. Res. 74(1), 1969.

Butterworth, S. (1930) On the theory of filter amplifiers, *Experimental Wireless & the Wireless Engineer*, *7*, 536-541.

Chen, M.W., M.S. Schulz, L.R. Lyons, and D.J. Gorney, Ion radial diffusion in an electrostatic impulse model for stormtime ring current formation, *Geophys. Res. Lett., 19*(6), 621-624, 1992.

Chen, X.-R., Q.-G. Zong, X.-Z. Zhou, J. B. Blake, J. R. Wygant, and C. A. Kletzing (2017), Van Allen Probes observation of a 360° phase shift in the flux modulation of injected electrons by ULF waves, *Geophys. Res. Lett., 44*, 1614–1624, doi:10.1002/2016GL071252.

Claudepierre, S. G., et al. (2013), Van Allen Probes observation of localized drift resonance between poloidal mode ultra-low frequency waves and 60 keV electrons, *Geophys. Res. Lett., 40*, 4491–4497, doi:10.1002/grl.50901.

Claudepierre SG, Blake JB, Boyd AJ, et al. (2021) The Magnetic Electron Ion Spectrometer: A Review of On-Orbit Sensor Performance, Data, Operations, and *Science. Space Sci. Rev.* doi:10.1007/s11214-021-00855-2, in press

Cornwall, J. M., (1968) Diffusion processes influenced by conjugate-point wave phenomena, Radio Sci., 3, 740-4, 10.1002/rds196837740

Cornwall, J. M. (1972), Radial diffusion of ionized helium and protons: A probe for magnetospheric dynamics, J. Geophys. Res., 77(10), 1756–1770, doi:10.1029/JA077i010p01756.

Dessler, A. J., and R. Karplus (1961), Some effects of diamagnetic ring currents on Van Allen radiation, *J. Geophys. Res., 66*(8), 2289–2295, doi:10.1029/JZ066i008p02289.

Elkington, S. R., M. K. Hudson, and A. A. Chan (2003), Resonant acceleration and diffusion of outer zone electrons in an asymmetric geomagnetic field, *J. Geophys. Res., 108*, 1116, doi:10.1029/2001JA009202, A3.

Falthammar,C.-G.,(1965).Effects of time-dependent electric fields on geomagnetically trapped radiation. J. Geophys. Res., 70 (11),2503.

Falthammar, C.-G., Radial diffusion by violation of the third adiabatic invariant, p. 157, in Earth's Particles and Fields, edited by B. M. McCormac, Reinhold Publishing Corp., New York, 1968.

Fei, Y., A. A. Chan, S. R. Elkington, and M. J. Wiltberger (2006), Radial diffusion and MHD particle simulations of relativistic electron transport by ULF waves in the September 1998 storm, *J. Geophys. Res., 111*, A12209, doi:10.1029/2005JA011211.

Foster, J. C., J. R. Wygant, M. K. Hudson, A. J. Boyd, D. N. Baker, P. J. Erickson, and H. E. Spence (2015), Shock-induced prompt relativistic electron acceleration in the inner magnetosphere, *J. Geophys. Res. Space Physics, 120*, 1661–1674, doi:10.1002/2014JA020642.

Glauert, S. A., R. B. Horne, and N. P. Meredith (2014), “Three-dimensional electron radiation belt simulations using the BAS Radiation Belt Model with new diffusion models for chorus, plasmaspheric hiss, and lightning-generated whistlers,” *J. Geophys. Res. Space Physics*, 119, 268–289, doi:10.1002/2013JA019281.

Hao, Y. X., Zong, Q.-G., Zhou, X.-Z., Rankin, R., Chen, X. R., Liu, Y., et al. (2019). Global-scale ULF waves associated with SSC accelerate magnetospheric ultrarelativistic electrons. *Journal of Geophysical Research: Space Physics, 124*, 1525–1538. https://doi.org/10.1029/2018JA026134

Hao, Y. X., Zhao, X. X., Zong, Q.-G., Zhou, X.-Z., Rankin, R., Chen, X. R., et al. (2020). Simultaneous observations of localized and global drift resonance. *Geophysical Research Letters, 47*, e2020GL088019. https://doi.org/10.1029/2020GL088019

Hartinger, M. D., Claudepierre, S. G., Turner, D. L., Reeves, G. D., Breneman, A., Mann, I. R., et al. (2018). Diagnosis of ULF wave-particle interactions with megaelectron volt electrons: The importance of ultrahigh-resolution energy channels. *Geophysical Research Letters, 45*, 10,883–10,892. https://doi.org/10.1029/2018GL080291

Hartinger, M. D., Reeves, G. D., Boyd, A., Henderson, M. G., Turner, D. L., Komar, C. M., et al. (2020). Why are there so few reports of high-energy electron drift resonances? Role of radial phase space density gradients. *Journal of Geophysical Research: Space Physics*, *125*, e2020JA027924. https://doi.org/ 10.1029/2020JA027924

Huang, C.-L., H. E. Spence, M. K. Hudson, and S. R. Elkington (2010), Modeling radiation belt radial diffusion in ULF wave fields: 2. Estimating rates of radial diffusion using combined MHD and particle codes, *J. Geophys. Res.*, 115, A06216, doi:10.1029/2009JA014918.

Hudson, M., A. Jaynes, B. Kress, Z. Li, M. Patel, X. Shen, S. Thaller, M. Wiltberger, and J. Wygant (2017), Simulated prompt acceleration of multi-MeV electrons by the 17 March 2015 interplanetary shock, *Journal of Geophysical Research: Space Physics, 122*, 10, doi:10.1002/2017ja024445.

Hudson, M.K, S.R. Elkington, Z. Li, and M. Patel (2020), Drift echoes and flux oscillations: A signature of prompt and diffusive changes in the radiation belts, *J. of Atmospheric and Solar-Terrestrial Physics, 207*, doi:10.1016/j.jastp.2020.105332

Jaynes, A. N., Ali, A. F., Elkington, S. R., Malaspina, D. M., Baker, D. N., Li, X., et al. (2018). Fast diffusion of ultrarelativistic electrons in the outer radiation belt: 17 March 2015 storm event. *Geophysical Research Letters, 45*, 10,874–10,882. https://doi.org/10.1029/2018GL07978

King, J.H., and N.E. Papitashvili (2005), Solar wind spatial scales in and comparisons of hourly Wind and ACE plasma and magnetic field data, *J. Geophys. Res., Vol. 110*, No. A2, A02209, 10.1029/2004JA010649.

Kletzing, C. et al. (2013), The electric and magnetic field instrument suite and integrated science (EMFISIS) on RBSP, *Space Sci. Rev.*, doi:10.1007/s11214-013-9993-6.

Kokubun, S., M.G. Kivelson, R.L. McPherron, and C.T. Russell, OGO 5 observations of Pc 5 waves: Particle flux modulations, J. Geophys. Res. 82(19), 2744-2786, 1977.

Kress, B. T., M. K. Hudson, M. D. Looper, J. Albert, J. G. Lyon, and C. C. Goodrich (2007), Global MHD test particle simulations of >10 MeV radiation belt electrons during storm sudden commencement, J. Geophys. Res., 112, A09215, doi:10.1029/2006JA012218.

Lanzerotti, L. J., C. G. Maclennan, and M. Schulz (1970), Radial diffusion of outer-zone electrons: An empirical approach to third-invariant violation, *J. Geophys. Res., 75*(28), 5351–5371, doi:10.1029/JA075i028p05351.

Lanzerotti, L. J., and C. G. Morgan (1973), ULF geomagnetic power near L = 4: 2. Temporal variation of the radial diffusion coefficient for relativistic electrons, *J. Geophys. Res., 78(22)*, 4600–4610, doi:10.1029/JA078i022p04600.

Lanzerotti, L.J., C.S. Roberts, and W.L. Brown (1969) Temporal variations in the electron flux at synchronous altitudes, *J. Geophys. Res., 72*(23).

Lanzerotti, L. J., D. C. Webb, and C. W. Arthur (1978), Geomagnetic field fluctuations at synchronous orbit 2. Radial diffusion, J. Geophys. Res., 83(A8), 3866–3870, doi:10.1029/JA083iA08p03866.

Lanzerotti, L., and A. Wolfe (1980), Particle diffusion in the geomagnetosphere: Comparison of estimates from measurements of magnetic and electric field fluctuations, *J. Geophys. Res., 85*(A5), 2346–2348, doi:10.1029/JA085iA05p02346.

Lejosne, S., D. Boscher, V. Maget, and G. Rolland (2013), Deriving electromagnetic radial diffusion coefficients of radiation belt equatorial particles for different levels of magnetic activity based on magnetic field measurements at geostationary orbit, *J. Geophys. Res. Space Physics, 118*, 3147–3156, doi:10.1002/jgra.50361.

Li, X., Roth, I., Temerin, M., Wygant, J.R., Hudson, M.K., Blake, J.B., 1993. Simulation of the March 9, 1985 prompt energization and transport of radiation belt particles during the March 24, 1991 SSC. Geophysical Research Letters 20, 2423.

Li, Z., M. Hudson, J. Paral,M. Wiltberger, and D. Turner (2016), Global ULF wave analysis of radial diffusion coefficientsusing a global MHD model for the17 March 2015 storm, *J. Geophys.Res. Space Physics, 121*, 6196–6206, doi:10.1002/2016JA022508.

Loto'aniu, T. M., I. R. Mann, L. G. Ozeke, A. A. Chan, Z. C. Dent, and D. K. Milling (2006), Radial diffusion of relativistic electrons into the radiation belt slot region during the 2003 Halloween geomagnetic storms, *J. Geophys. Res., 111*, A04218, doi:10.1029/2005JA011355.

Loto'aniu, T. M., H. J. Singer, C. L. Waters, V. Angelopoulos, I. R. Mann, S. R. Elkington, and J. W. Bonnell (2010), Relativistic electron loss due to ultralow frequency waves and enhanced outward radial diffusion, *J. Geophys. Res., 115*, A12245, doi:10.1029/2010JA015755.

Mann, I. R., et al. (2008), The upgraded CARISMA magnetometer array in the THEMIS era, *Space Sci. Rev., 141*, 413–451, doi:10.1007/s11214-008-9457-6.

Mann, I. R., L. G. Ozeke, K. R. Murphy, S. Claudepierre, D. L. Turner, D. N. Baker, I. J. Rae, A. Kale, D. Milling, and A. Boyd (2016), Explaining the dynamics of the ultra-relativistic third Van Allen radiation belt, *Nat. Phys.*, doi:10.1038/nphys3799.

Mauk, B. H., N. J. Fox, S. G. Kanekal, R. L. Kessel, D. G. Sibeck, and A. Ukhorskiy (2013), Science objectives and rationale for the Radiation Belt Storm Probes mission, *Space Sci. Rev., 179*, 3–27, doi:10.1007/s11214-012-9908-y.

O'Brien, T. P. (2015), The activity and radial dependence of anomalous diffusion by pitch angle scattering on split magnetic drift shells, *J. Geophys. Res. Space Physics, 120*, 328–343, doi:10.1002/2014JA020422.

Olson, W.P. and K.A. Pfitzer (1977) Magnetospheric magnetic field modeling, Annual Scientific Report, Air Force Office of Scientific Research contract F44620-75-C-0033, McDonnell Douglas Astronautics Co., Huntington Bech, CA.

Ozeke, L. G., I. R. Mann, K. R. Murphy, I. Jonathan Rae, and D. K. Milling (2014), Analytic expressions for ULF wave radiation belt radial diffusion coefficients, *J. Geophys. Res. Space Physics*, *119*, 1587–1605, doi:10.1002/2013JA019204.

Ozeke, L. G., I. R. Mann, K. R. Murphy, I. J. Rae, D. K. Milling, S. R. Elkington, A. A. Chan, and H. J. Singer (2012), ULF wave derived radiation belt radial diffusion coefficients, *J. Geophys. Res.*, *117*, A04222, doi:10.1029/2011JA017463.

Ozeke, L. G., I. R. Mann, K. R. Murphy, D. G. Sibeck, and D. N. Baker (2017), Ultra-relativistic radiation belt extinction and ULF wave radial diffusion: Modeling the September 2014 extended dropout event, *Geophys. Res. Lett.*, *44*, 2624–2633, doi:10.1002/2017GL072811.

Ozeke, L. G., Mann, I. R., Claudepierre, S. G., Henderson, M., Morley, S. K., Murphy, K. R., et al. (2019). The March 2015 superstorm revisited: Phase space density profiles and fast ULF wave diffusive transport. *Journal of Geophysical Research: Space Physics*, *124*, 1143–1156. https://doi.org/10.1029/2018JA026326

Ozeke, L. G., Mann, I. R., Dufresne, S. K. Y., Olifer, L., Morley, S. K., Claudepierre, S. G., et al. (2020). Rapid outer radiation belt flux dropouts and fast acceleration during the March 2015 and 2013 storms: The role of ULF wave transport from a dynamic outer boundary. *Journal of Geophysical Research: Space Physics*, *125*, e2019JA027179. https://doi.org/10.1029/2019JA027179

Patel, M., Li, Z., Hudson, M., Claudepierre, S., & Wygant, J. (2019). Simulation of prompt acceleration of radiation belt electrons during the 16 July 2017 storm. *Geophysical Research Letters*, *46*, 7222–7229. https://doi.org/10.1029/2019GL083257

Reeves, G. D., Y. Chen, G. S. Cunningham, R. W. H. Friedel, M. G. Henderson, V. K. Jordanova, J. Koller, S. K. Morley, M. F. Thomsen, and S. Zaharia (2012), Dynamic Radiation Environment Assimilation Model: DREAM, *Space Weather*, *10*, S03006, doi:10.1029/2011SW000729.

Reeves, G. D., K. L. McAdams, R. H. W. Friedel, and T. P. O'Brien (2003), Acceleration and loss of relativistic electrons during geomagnetic storms, *Geophys. Res. Lett.*, *30*, 1529, doi:10.1029/2002GL016513, 10.

Riley, P., and R.A. Wolf, Comparison of diffusion and particle drift descriptions of radial transport in the Earth’s inner magnetosphere, *J. Geophys. Res.*, *97* (A11), 16,865, 1992.

Sandhu, J. K., Rae, I. J., Wygant, J. R., Breneman, A. W., Tian, S., Watt, C. E. J., et al. (2021). ULF wave driven radial diffusion during geomagnetic storms: A statistical analysis of Van Allen Probes observations. *Journal of Geophysical Research: Space Physics*, *126*, e2020JA029024. https://doi.org/10.1029/2020JA029024

Sarris, T. E., X. Li, and M. Temerin (2006), Simulating radial diffusion of energetic (MeV) electrons through a model of fluctuating electric and magnetic fields, Ann. Geophys., 24, 1–16, doi:10.5194/angeo-24-2583-2006.

Sarris, T. E., Li, X., Temerin, M., Zhao, H., Khoo, L. Y., Turner, D. L., et al. (2020). Simulations of electron flux oscillations as observed by MagEIS in response to broadband ULF waves. *Journal of Geophysical Research: Space Physics*, *125*, e2020JA027798. https://doi.org/10.1029/2020JA027798

Sarris, T. E., Li, X., Zhao, H., Khoo, L. Y., Liu, W., & Temerin, M. A. (2021). On the association between electron flux oscillations and local phase space density gradients. *Journal of Geophysical Research: Space Physics*, *126*, e2020JA028891. https://doi.org/10.1029/2020JA028891

Schulz, M., The magnetosphere, *Geomagnetism,* 4, 87-293, 1991.

Schulz, M., and Lanzerotti, L. J. (1974), Physics and Chemistry in Space, *Particle Diffusion in the Radiation Belts, vol. 7.*, Springer, New York.

Shprits, Y.Y., Thorne, R.M. (2004)Time dependent radial diffusion modeling of relativistic electrons with realistic loss rates. *Geophysical Research Letters, 31*, L08805.

Shprits, Y.Y., Thorne, R.M., Friedel, R., Reeves, G.D., Fennell, J., Baker, D.N., Kanekal, S.G., (2006) Outward radial diffusion driven by losses at magnetopause, *Journal of Geophysical Research, 111*, A11214.

Sorathia, K. A., Ukhorskiy, A. Y., Merkin, V. G., Fennell, J. F., & Claudepierre, S. G. (2018). Modeling the depletion and recovery of the outer radiation belt during a geomagnetic storm: Combined MHD and test particle simulations. *Journal of Geophysical Research: Space Physics*, *123*, 5590–5609. https://doi.org/10.1029/2018JA025506

Southwood, D. J., and M. G. Kivelson (1981), Charged particle behavior in low-frequency geomagnetic pulsations 1. Transverse waves, *J. Geophys. Res.*, *86*(A7), 5643–5655, doi:10.1029/JA086iA07p05643.

Spence, H. E., et al. (2013), Science goals and overview of the Radiation Belt Storm Probes (RBSP) Energetic Particle, Composition, and Thermal Plasma (ECT) suite on NASA's Van Allen Probes mission, Space Sci. Rev., 179(1–4), 311–336, doi:10.1007/s11214-013-0007-5.

Su, Z., F. Xiao, H. Zheng, and S. Wang (2011), Radiation belt electron dynamics driven by adiabatic transport, radial diffusion, and wave-particle interactions, *J. Geophys. Res., 116*, A04205, doi:10.1029/2010JA016228.

Subbotin, D. A., and Y. Y. Shprits (2009), Three-dimensional modeling of the radiation belts using the Versatile Electron Radiation Belt (VERB) code, *Space Weather, 7*, S10001, doi:10.1029/2008SW000452.

Teramoto, M., Hori, T., Saito, S., Miyoshi, Y., Kurita, S., Higashio, N., et al. (2019). Remote detection of drift resonance between energetic electrons and ultralow frequency waves: Multisatellite coordinated observation by Arase and Van Allen Probes. *Geophysical Research Letters*, *46*, 11,642-11,651. https://doi.org/10.1029/2019GL084379

Tsyganenko, N. A., and M. I. Sitnov (2005), Modeling the dynamics of the inner magnetosphere during strong geomagnetic storms, *J. Geophys. Res.*, 110, A03208, doi:10.1029/2004JA010798.

Tu, W., G. S. Cunningham, Y. Chen, M. G. Henderson, E. Camporeale, and G. D. Reeves (2013), Modeling radiation belt electron dynamics during GEM challenge intervals with the DREAM3D diffusion model, *J. Geophys. Res. Space Physics*, 118, 6197–6211, doi:10.1002/jgra.50560.

Ukhorskiy, A. Y., B. J. Anderson, K. Takahashi, and N. A. Tsyganenko (2006), Impact of ULF oscillations in solar wind dynamic pressure on the outer radiation belt electrons, *Geophys. Res. Lett.*, *33*, L06111, doi:10.1029/2005GL024380.

Ukhorskiy, A.Y., and M.I. Sitnov, (2008), Radial transport in the outer radiation belt due to global magnetospheric compressions, *JASTP*, *70*, 1714-1726, doi:10.1016/j.jastp.2008.07.018.

Ukhorskiy, A., & Sitnov, M. (2012). Dynamics of radiation belt particles. The Van Allen probes mission, Springer pp. 545–578.

Zhao, H., Sarris, T. E., Li, X., Weiner, M., Huckabee, I. G., Baker, D. N., et al. (2021). Van Allen Probes observations of multi-MeV electron drift-periodic flux oscillations in Earth's outer radiation belt during the March 2017 event. *Journal of Geophysical Research: Space Physics*, *126*, e2021JA029284. https://doi.org/10.1029/2021JA029284

Zong, Q.-G., X.-Z. Zhou, Y. F. Wang, X. Li, P. Song, D. N. Baker, T. A. Fritz, P. W. Daly, M. Dunlop, and A. Pedersen (2009), Energetic electron response to ULF waves induced by interplanetary shocks in the outer radiation belt, *J. Geophys. Res.*, *114*, A10204, doi:10.1029/2009JA014393.

Figure Captions:

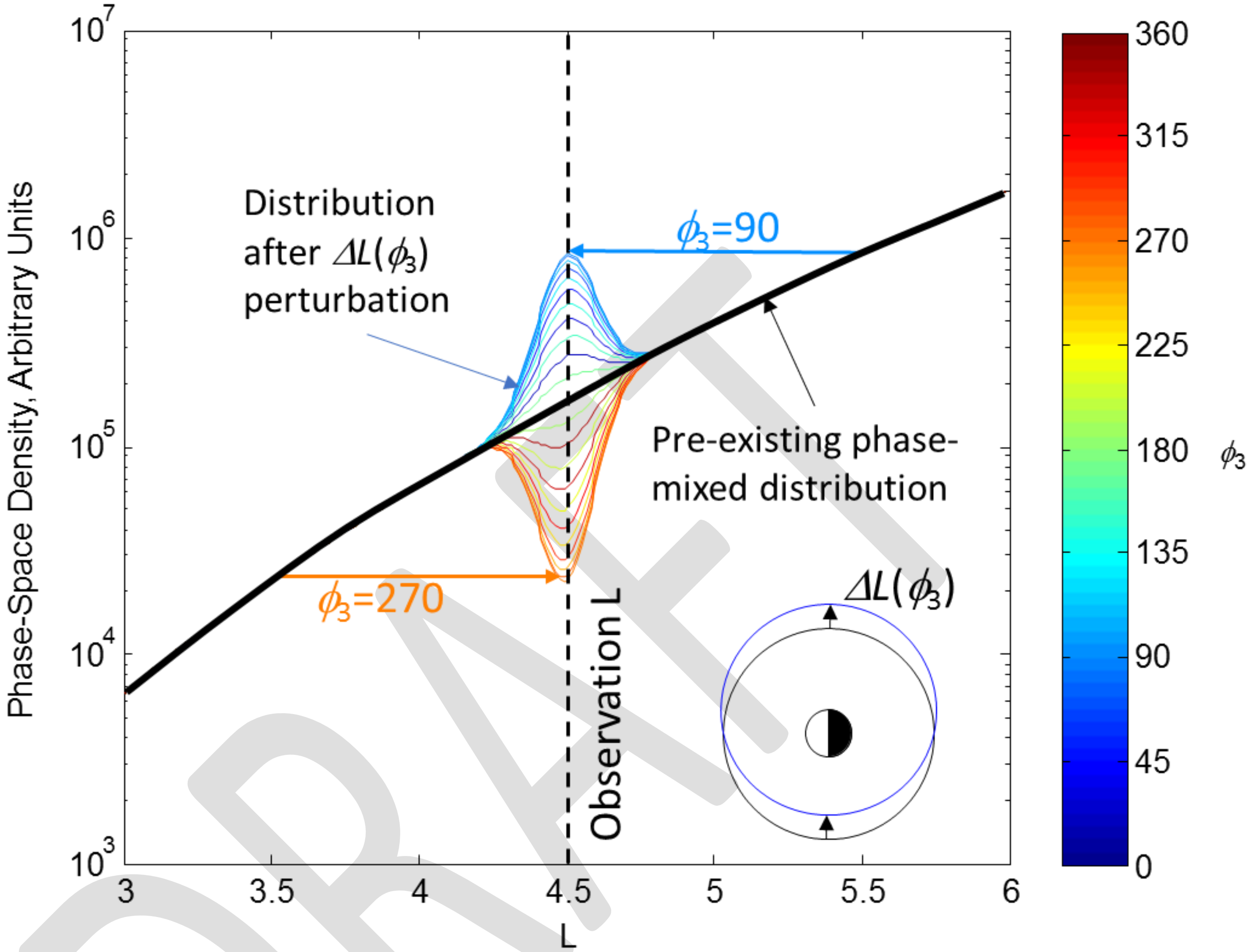

Figure 1. An illustration of how a radial offset that depends on drift phase can lead to drift phase structure. Particles at ϕ_3~90° are transported inward, and those at ϕ_3~270° are transported outward (see inset). Liouville's theorem says that they carry their phase space density (PSD) with them along their trajectories. This results in smooth, phase-mixed prior distribution producing a phase-dependent PSD at L=4.5.

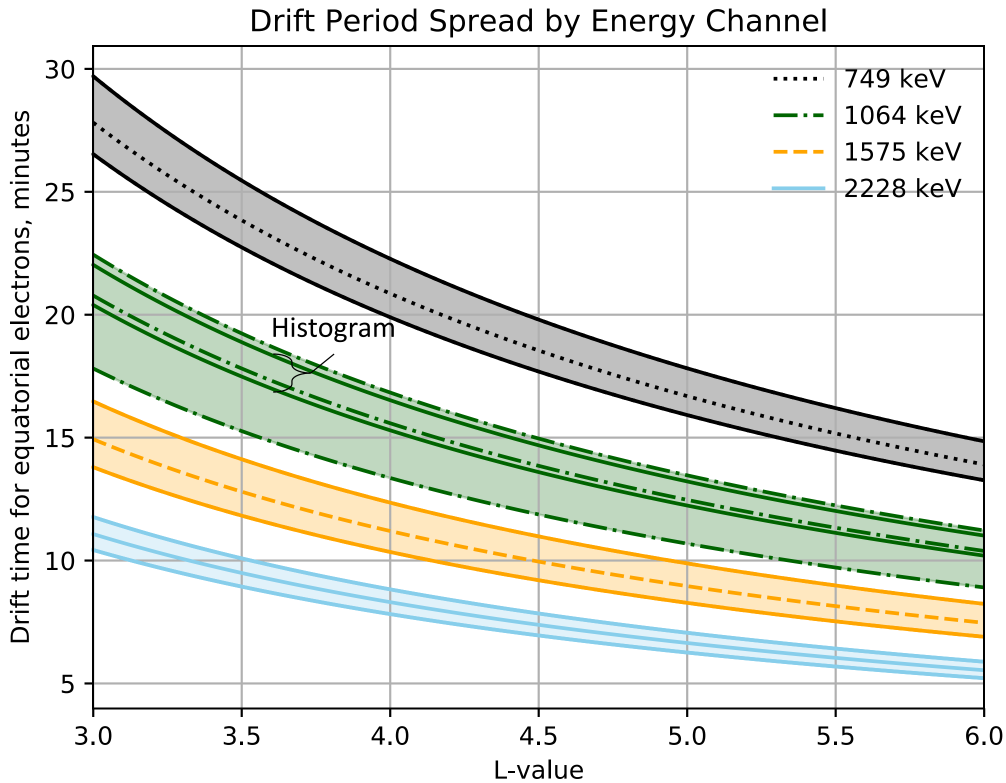

Figure 2. The *L*-dependence and bandwidth of the dipole drift period for the MagEIS electron energy channels used in this study. The 1064 keV channel is used as a broader main rate and a narrower histogram channel. The other three channels are only used in their main rate form. The color-filled bandwidth represents the full-width, half-max channel response. The drift period assumes equatorially mirroring electrons.

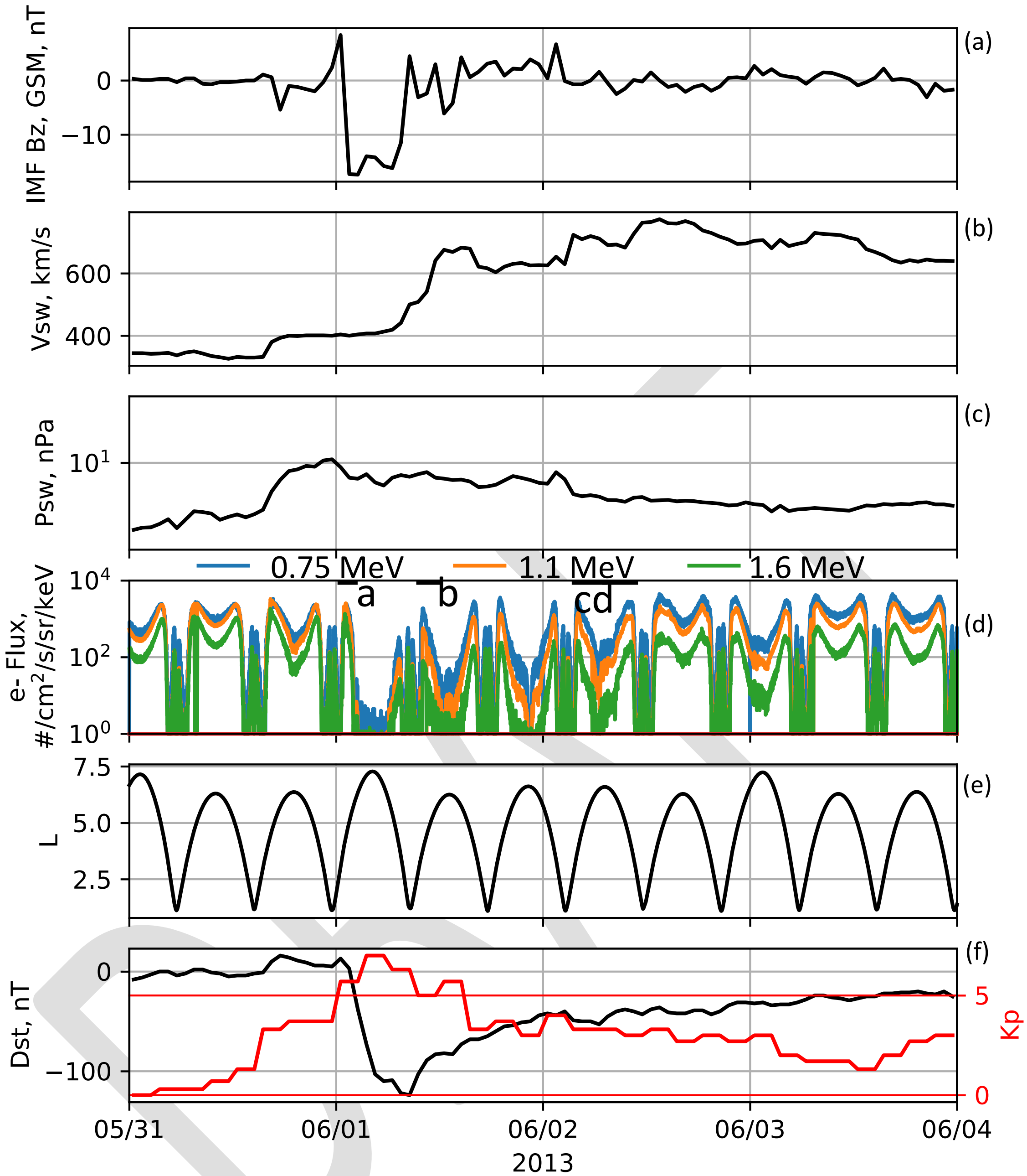

Figure 3. Overview of the June 2013 event. Panel (a) shows the north-south component of the interplanetary magnetic field (the z component in the geocentric, solar magnetospheric coordinate system). Panel (b) shows the solar wind speed. Panel (c) shows the solar wind dynamic pressure. Panel (d) shows locally mirroring flux for the four MagEIS electron channels and also contains horizontal black bars marking the four passes that will be studied in detail. Panel (e) provides the McIlwain *L* value (Olson-Pfitzer Quiet field model) of the RBSP-B spacecraft. Panel (f) shows the *Dst* index on the left axis and the *Kp* index on the right axis.

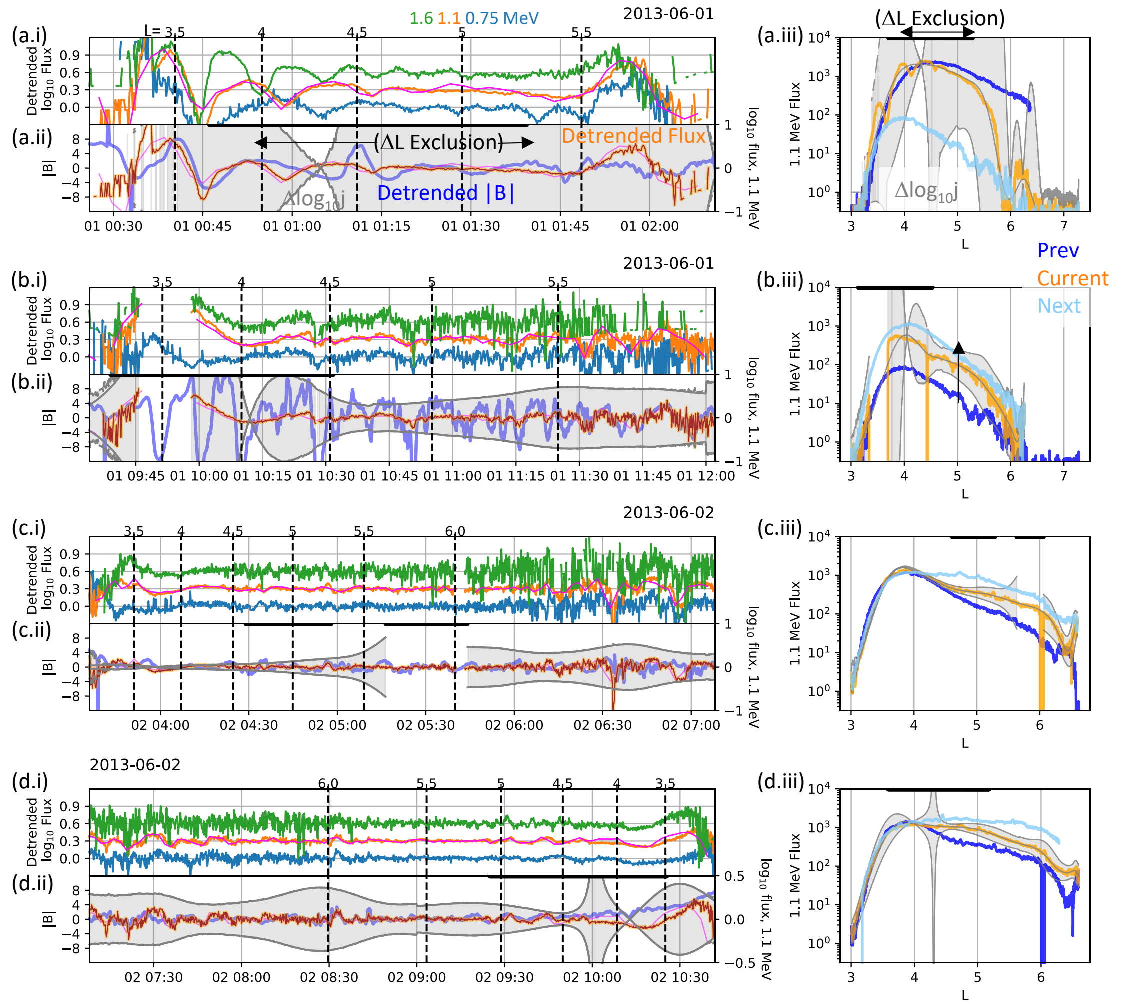

Figure 4. Four selected passes from the June 2013 event. Panel (a.i) shows the detrended $\log_{10}$ locally mirroring flux in the three MagEIS main channels (arbitrary units, vertically offset). The 1.1 MeV main channel is shown in orange, while a narrow-band histogram channel near the same energy is shown in magenta. Spacecraft L values are indicated. Panel (a.ii) shows the detrended magnetic field strength at RBSP-B (blue, left axis) and the detrended 1.1 MeV $\log_{10}$ locally mirroring flux (orange and magenta, right axis). Again, orange and magenta refer to the main and histogram channels. Gray shading indicates the $\pm\Delta \ln j$ boundaries. Panel (a.iii) shows three passes of 1.1 MeV MagEIS locally mirroring flux. The orange trace indicates observed 1.1 MeV flux the same pass shown panels a.i and a.ii. The dark blue shows that pass prior, and light blue shows the following pass. Gray shading indicates the $\pm\Delta \ln j$ boundaries. The black horizontal bars in (a.ii) and (a.iii) indicate where the change in L over one drift period is either less than 0.05 or greater than 0.5. Panels (b.i) through (d.ii) follow the same format as (a.i) through (a.iii), but present the other three passes noted in Figure 3.

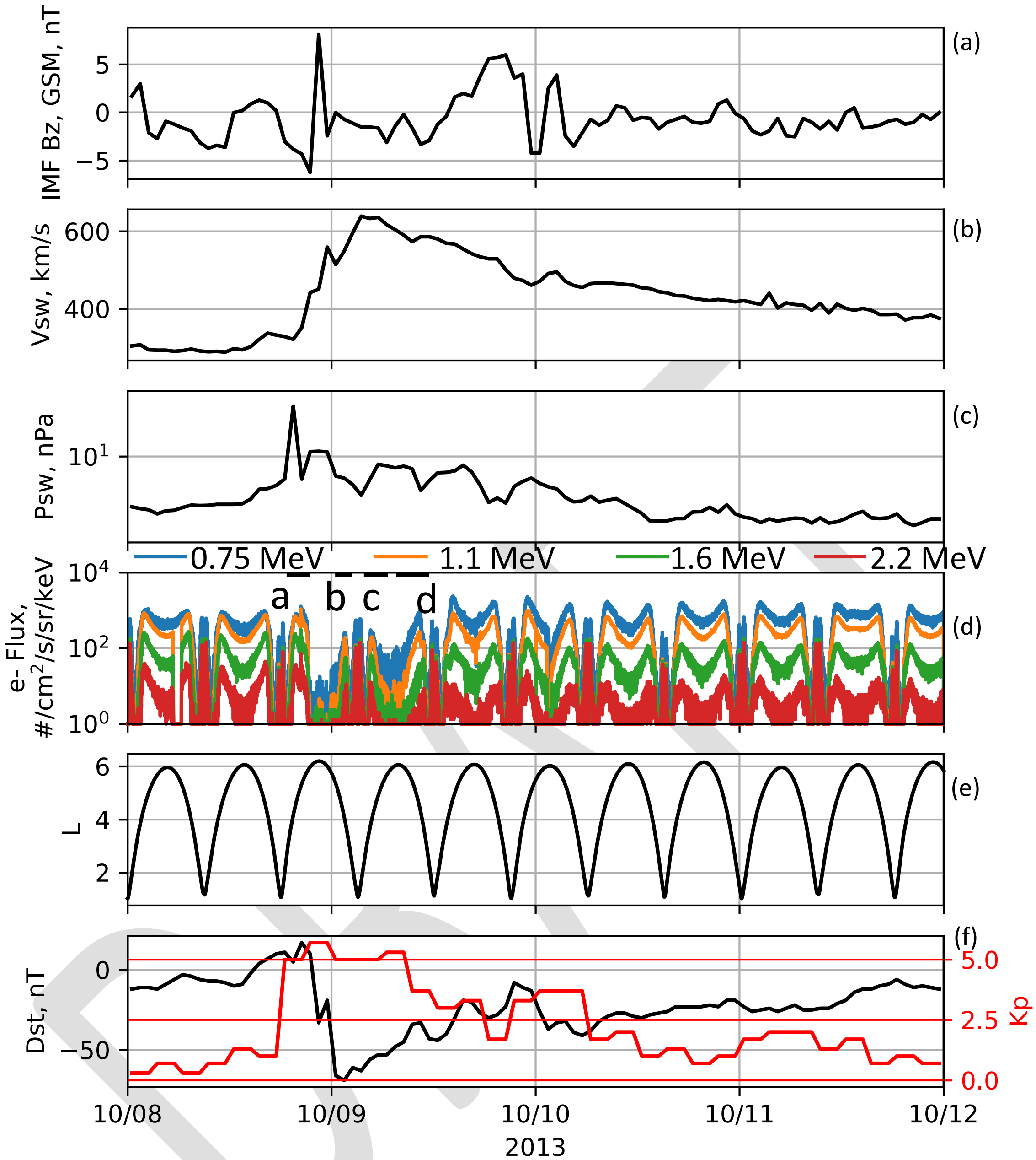

Figure 5. Overview of the October 2013 event in the same format as Figure 3.

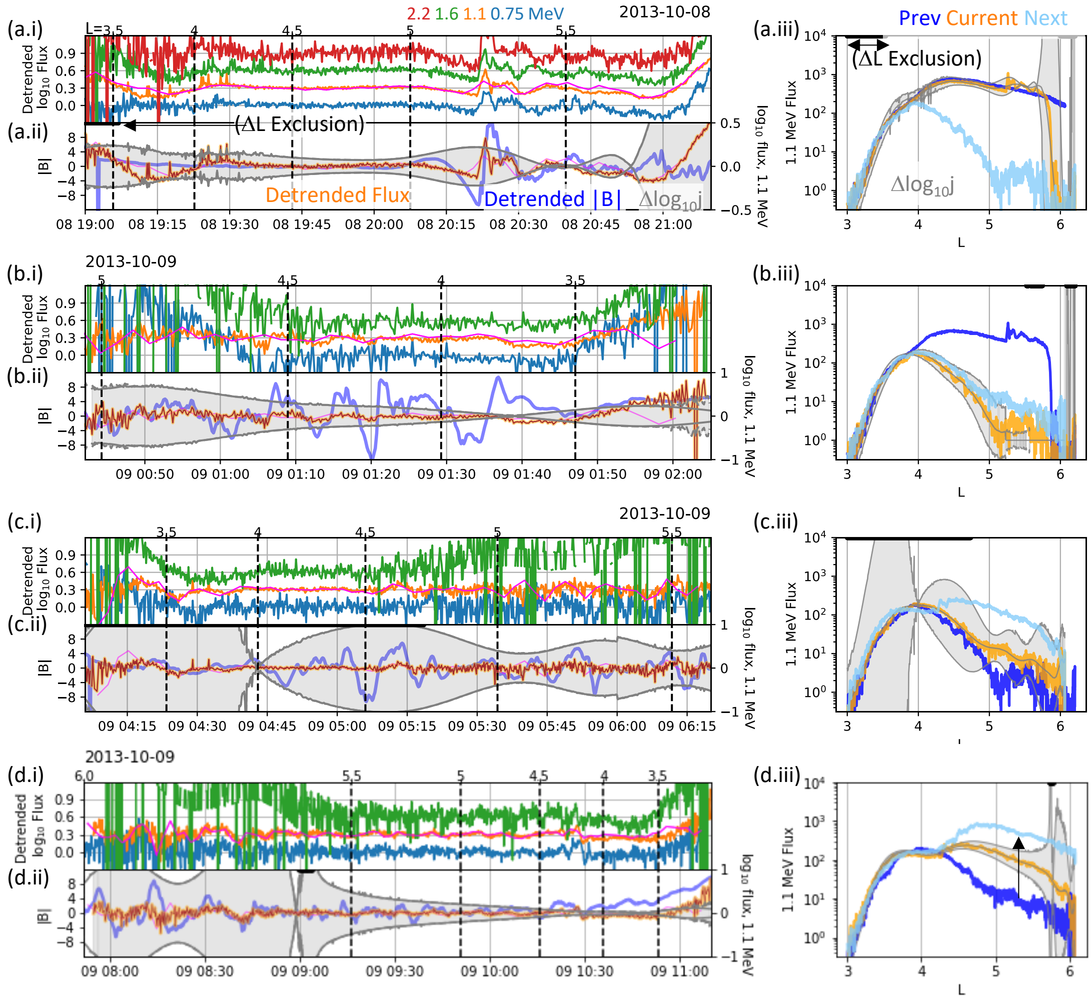

Figure 6. Four passes from the October 2013 event, in the same format as Figure 4, but with a fourth MagEIS energy channel added (2.2 MeV).

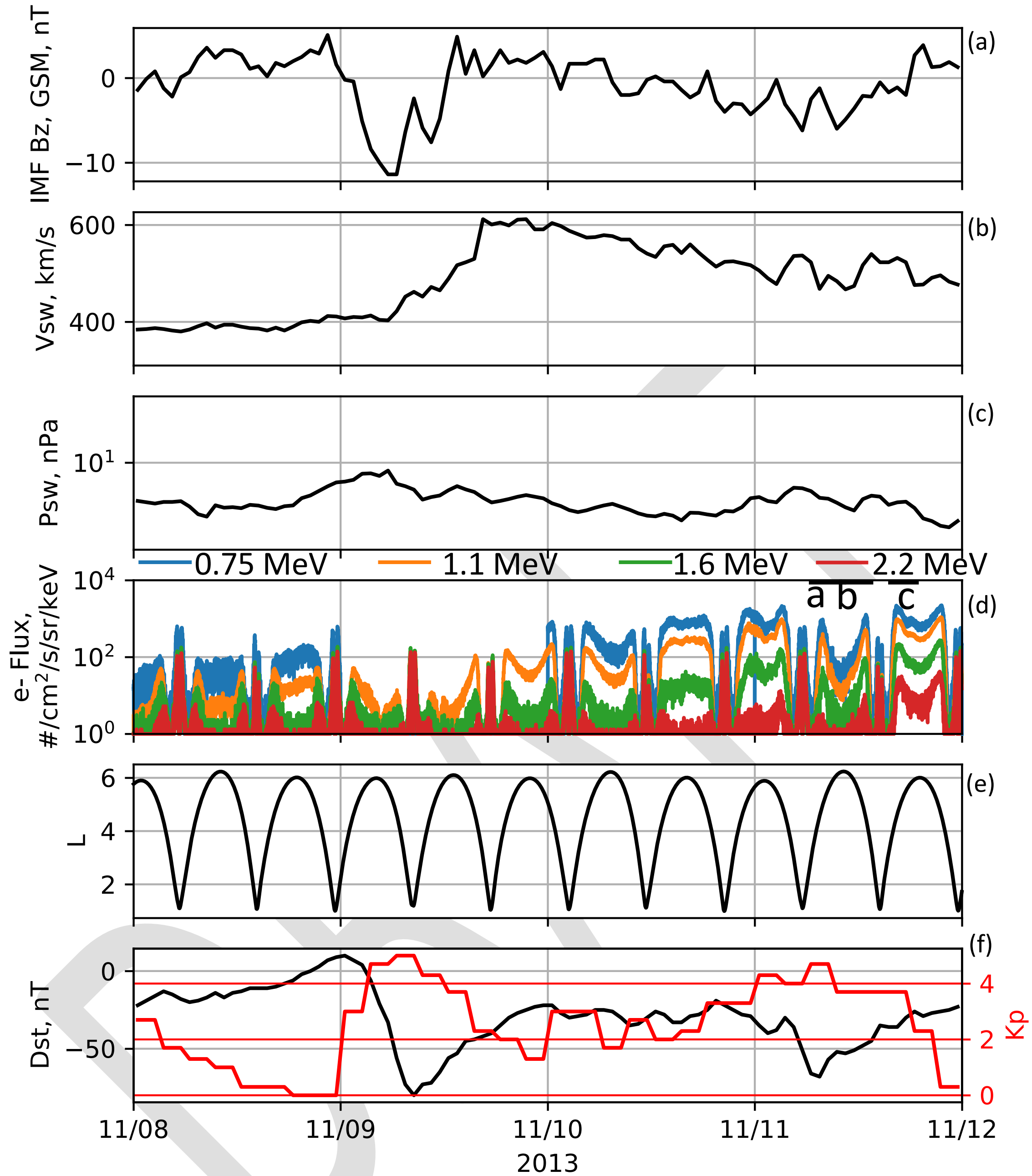

Figure 7. Overview of the November 2013 event in the same format as Figure 3.

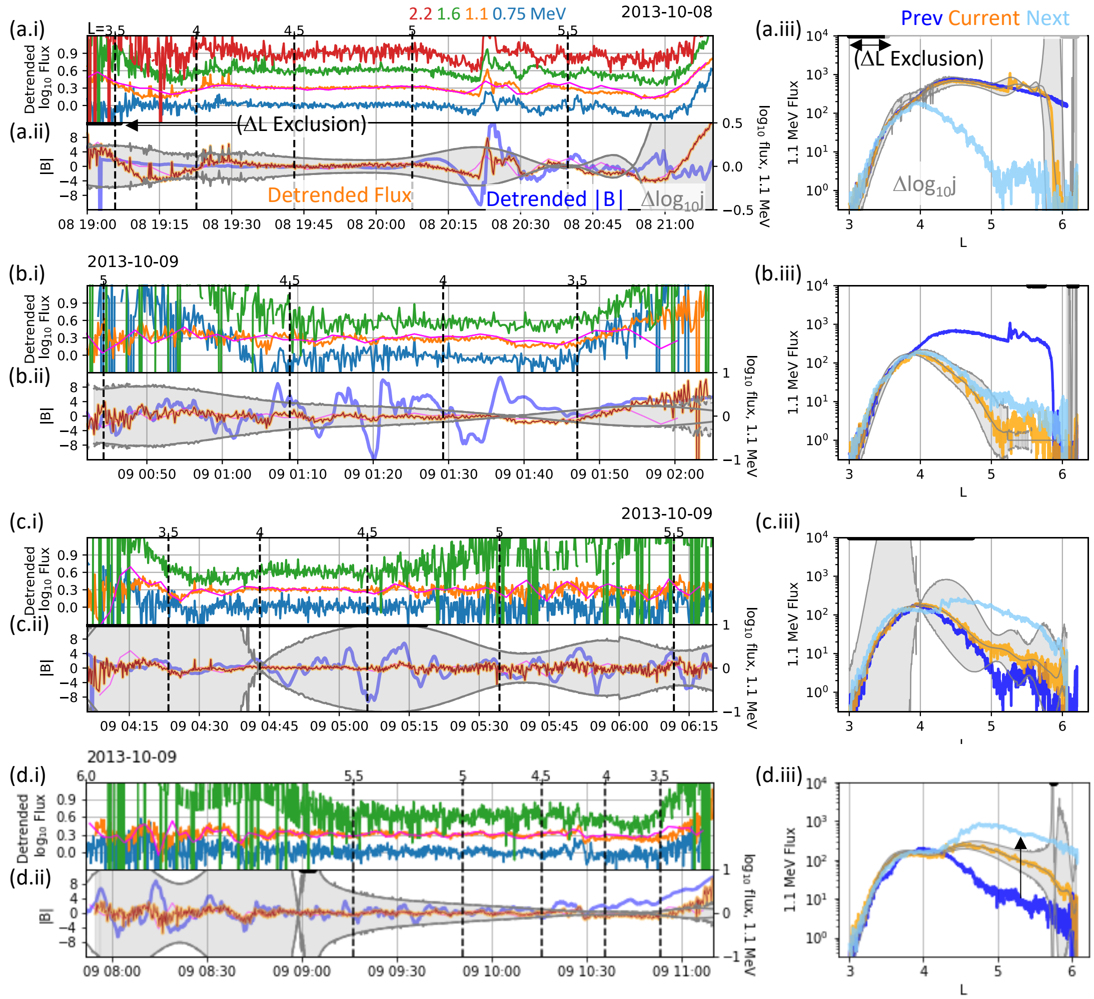

Figure 8. Three passes from the November 2013 event, in the same format as Figure 4.

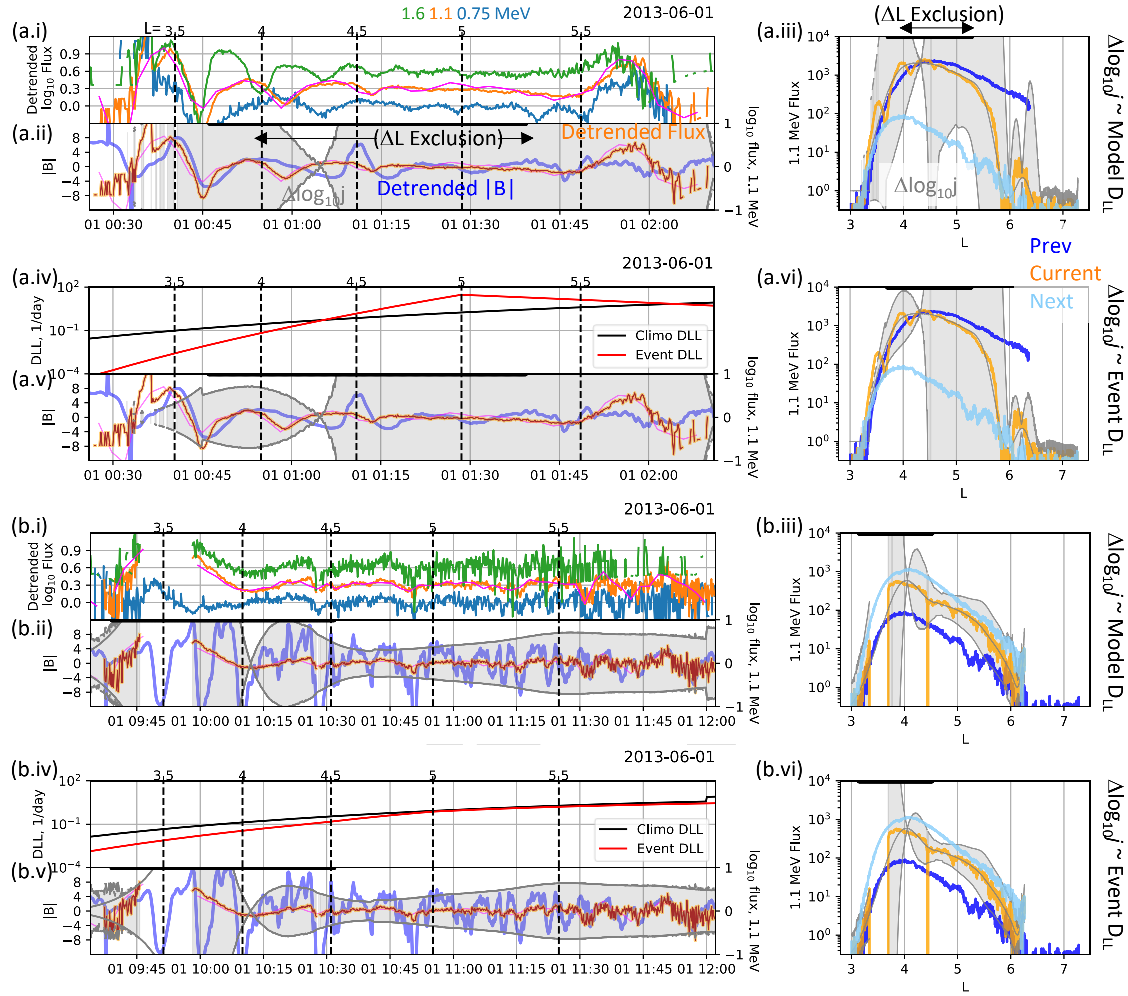

Figure 9. Four selected passes from the June 2013 event. Panels (a.i-a.iii) are repeated from Figure 4, showing pass *a* from 3. Panel (a.iv) compares D_{LL} for the *Ozeke et al.* [2014] climatological model to the event-specific D_{LL}. Panels (a.v) and (a.vi) follow the same format as panels (a.ii) and (a.iii), except using the event-specific D_{LL} to compute the $\pm\Delta \ln j$ boundaries. Panels (b.i-b.vi) follow the same pattern, showing pass *b* from Figure 3.